Environmental Science and Pollution Research (2023) 30:78692–78706
https://doi.org/10.1007/s11356-023-27867-5

RESEARCH ARTICLE

Visible light-driven photocatalytic bacterial inactivation on PPE, supported by the DFT and bactericidal study

Gulzar Ahmed[1] · Adeel Rasheed[2] · Khurram Shahzad Munawar[3] · Satesh Bandaru[4] · Javid Khan[5] · Zhongwu Liu[1] · Muhammad Sheraz Ahmad[6]

Received: 24 October 2022 / Accepted: 18 May 2023 / Published online: 5 June 2023

Abstract

A novel ZnO-MoO_3-$ZnMoO_3$@graphene GZM composite catalyst prepared by microwave hydrothermal process for personal protective equipment textiles (PPE) is presented in this study. The results indicated that the GZM with defect vacancy sites of two types as observed by EPR showed significantly superior inactivation of the *E. coli* bacteria compared to GZM without the lower defect vacancy sites and concomitant lower electron densities. Photocatalytic activated oxidation by the GZM composites coatings was observed to proceed in acceptable times as well as the bacterial inactivation (log bact. $C/C_o > 10^7$ within 3 h). Defect sites in the GZM seem to be important leading to the bacterial inactivation process. DFT calculations on the GZM with and without catalyst defect sites were carried out. The electron densities were estimated by the Fourier mapping. The results found in this study showed the potential of GZM-PPE for practical applications.

Keywords PPE · Bacteria inactivation · Heterogeneous catalysis · Electron density calculations · Photocatalysis · Fourier mapping

Introduction

All humans worldwide are increasingly cautious about the health problems originating from the bacteria and viruses such as COVID-19, Delta, Omicron and *E. coli*. Therefore, to develop safer PPEs with efficient protective properties against microscopic organisms is highly desirable (Mick and Murphy 2020). As an example, the family of Coronaviruses has imposed a serious threat to human health by causing several fatal diseases; hence, protective, and safe surfaces are highly important (Chang et al. 2020). The PPEs are widely useful for researchers, doctors, medical staff, teachers, students, government officials, tourists and workers.

Commonly used methods for bacteria and virus inactivation have not been hundred percent effective because of higher operating expenses and other problems (Cook 2020; Lotfi et al. 2020). Researchers are more interested in the wide-bandgap semiconductors and composite materials in the realm of photocatalysis to destroy microorganisms (Morawska et al. 2020). Major transmission of virus species among farms and human contact areas commonly occurs through aerial transmission (Suleyman et al. 2018). As a result, efficient technologies are required to eliminate these exceedingly dangerous microorganisms.

Responsible Editor: Sami Rtimi

✉ Gulzar Ahmed
gulzar.ahmed@uos.edu.pk

Javid Khan
javidchemist@yahoo.com

Zhongwu Liu
zwliu@scut.edu.cn

[1] School of Materials Science and Engineering, South China University of Technology, Guangzhou 510640, China

[2] Department of Physics, University of Mianwali, Mianwali 42200, Pakistan

[3] Institute of Chemistry, University of Sargodha, Sargodha 40100, Pakistan

[4] College of Material Science and Environmental Engineering, Hangzhou Dianzi University, Hangzhou 310018, China

[5] College of Material Science and Engineering, Hunan University, Changsha 410082, China

[6] Center for Environmental Sustainability and Human Health, Ming Chi University of Technology, New Taipei City 24301, Taiwan

Under UV light, the TiO_2 thin film may considerably eradicate the influenza virus in the air by breaking down viral proteins (Nakano et al. 2012). The TiO_2 photocatalysts ($\lambda > 410$ nm) loaded with Fe, Mg, and Mn were tested against influenza virus H1N1 under visible-light irradiation (Choi and Cho 2018). Within 30 min, this technique had eliminated nearly all of the bacteria. Kim and Jang recently employed vacuum UV (VUV) spiral-type Pd-TiO_2 catalysts to inactivate airborne MS2 viruses with shorter irradiation periods (0.004–0.125 s) (Kim and Jang 2018). These energy-saving discoveries showed that semiconductor-based photocatalysis may be used to eradicate pathogens. Earlier studies have elucidated the process of converting hazardous substances such as methylene blue to either less harmful intermediate compounds or non-toxic molecules through chemical detoxification (Kurniawan et al. 2020; Ahmed et al. 2016).

The nano ZnO is a strong candidate in catalysis for the inactivation of microorganisms (Taghizadeh et al. 2020). The antibacterial properties of ZnO originated from the infusion into the microorganism's cell membrane and the superoxides and peroxides damaged the DNA (Aydin Sevinç and Hanley 2010; Kairyte et al. 2013). Graphene oxide (GO) comprising hydroxyl and carboxyl groups exhibits the outstanding capability to make new bonds with various metal oxides for the synthesis of graphene oxide–based composites (Gao et al. 2013). Oxides and mixed phases of molybdenum are widely utilized as photocatalysts for a variety of oxidation reactions (Ramar and Karthikeyan 2021). Materials based on molybdenum (Mo) with rich electronic properties have been extensively researched for their potential in mitigating environmental pollution. These materials have been thoroughly investigated for their performance in photocatalysis, thermal catalysis, electrocatalysis, Fenton or Fenton-like reactions, and other technical methods, fully exploiting the unique properties of various Mo-based materials (Ji et al. 2021). Graphene as a substrate for their photocatalyst due to its unique properties, such as high surface area, excellent electrical conductivity, and high thermal stability (Huang et al. 2012). These properties make graphene an ideal substrate for various applications, including photocatalysis (Lu et al. 2021b). In addition, the use of graphene as a substrate can provide more transition sites for the photocatalyst, leading to improved efficiency in the photocatalytic reaction (Low et al. 2015). During the synthesis process, surface modification of a compound for better charge transfer and the presence of defects are integral parts of the active material's surface. Hydroxyl and carboxyl groups on the surface of GO may oxidize and the catalyst itself is reduced to generate a defect on the surface (Dhanabal et al. 2020). The L-MT heterostructure and CdS exhibit strong adsorption ability and high photocatalytic performance in the degradation of Congo red and RhB dye that obviously revealed an efficient photocatalyst for environmental applications (Ramalingam et al. 2022; Gopal et al. 2020).

In this study, the final phase of photocatalyst (ZnO-MoO_3)@graphene was distinguished as the major phase with a minor phase as $ZnMoO_3$. As a result, the phase transition of MoO_3 and graphene hybrid composites (ZnO-MoO_3)@graphene (GZM composites) might improve charge transfer capabilities in photocatalysis. Theoretical calculations were performed to understand the charge transfer mechanism. The electron density and Fourier mapping supported experimental results such as PXRD, XPS, EIS and EPR.

Experimental section

$Zn(NO_3)_2{\cdot}6H_2O$, NH_4OH, ammonium molybdate tetrahydrate $(NH_4)_6Mo_6O_{24}{\cdot}4H_2O$, ethylene glycol($C_2H_6O_2$), t-BuOH, ethanol, N_2, tetraethyl orthosilicate, and EDTA-2Na, sodium chromate (Cr(VI)), superoxide dismutase, L-histidine, catalase, isopropanol and sodium oxalate were all obtained from RichJoint Chemical Reagent Co., Ltd. (Shanghai, China) and graphene oxide from XFNANO company Nanjing. All the chemical reagents were used without further purification. The deionized water was prepared in the laboratory prior to the synthesis.

Photocatalyst synthesis

ZnO and MoO_3 synthesis

ZnO nanoparticles with uniform size were prepared by the co-precipitation technique. 0.1 mol/L aqueous solution of Zinc nitrate hexahydrate $Zn(NO_3)_2{\cdot}6H_2O$ was prepared and ammonium hydroxide was added dropwise with a dropper under constant stirring to obtain the P^H 8. Then, the white precipitates obtained by the centrifugation were dispersed in 30 mL of ethylene glycol($C_2H_6O_2$), and heated at 50 °C for 10 h. Ethylene glycol (EG) can serve as a solvent and a reducing agent in the synthesis of ZnO nanoparticles. In the synthesis process, EG is typically used as a reaction medium and a capping agent, which controls the particle size, shape, crystallinity and prevents the nanoparticles from agglomerating. The precipitate was washed three times with distilled water and ethanol, then centrifuged at 4000 rpm for 5 min and dried at 50 °C for 12 h. Then for MoO_3 nanoparticles, a stoichiometric amount of ammonium molybdate tetrahydrate $(NH_4)_6Mo_6O_{24}{\cdot}4H_2O$ in 0.9 mL of NH_4OH was added and stirred for 8 h. The as formed precipitates were filtrated, washed with DI water and dried in air at 60 °C for 12 h. Finally, the prepared samples were calcined at 300 °C for 3 h with a heating rate of 2 °C min^{-1}.

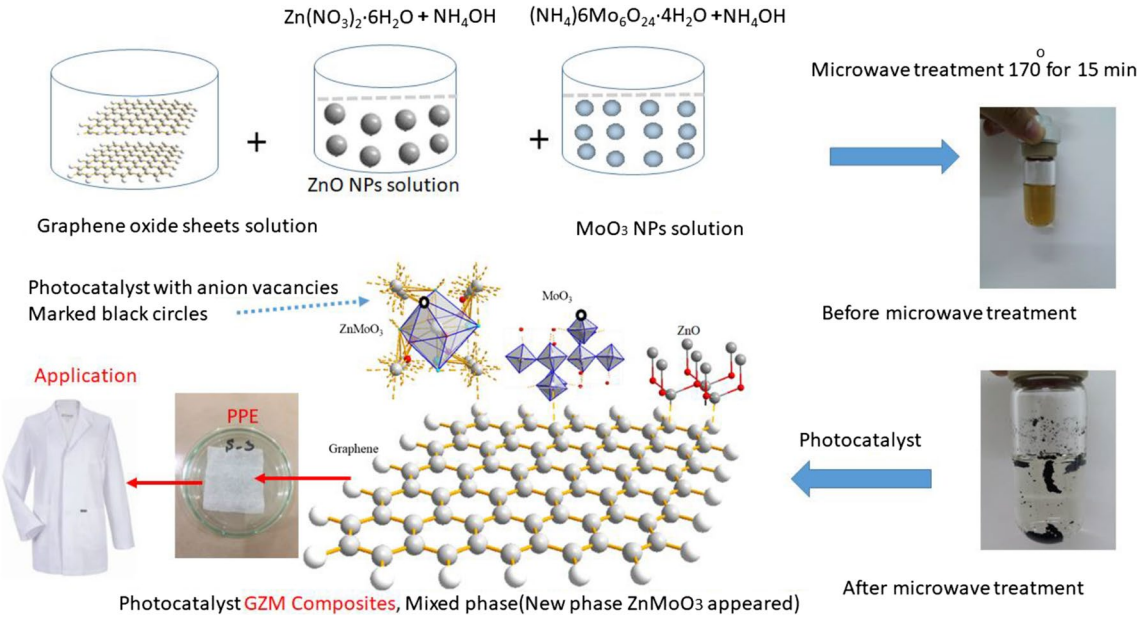

Scheme 1 Schematic representation for the synthesis of (ZnO-MoO_3-$ZnMoO_4$)@rGO GZM nanocomposite catalysts

(ZnO-MoO_3-$ZnMoO_3$)@graphene GZM synthesis

ZnO nanoparticles, MoO_3 and graphene oxide (GO) containing weight ratios of 85%, 5% and 10%, respectively, were mixed and sonicated for 60 min to get a uniform suspension. 10 mL of the mixed solution was poured into a microwave glass-tube, sealed and heated in a microwave reactor (NOVA-2S) at 170 °C for 15 min. After that, the microwave reactor was cooled down to 70 °C. The black precipitate was collected and washed with DI water, then dried at 80 °C for 6 h. The final product of (ZnO-MoO_3-$ZnMoO_3$)@rGO composites was defined as GZM composites in this work (Scheme 1).

Fabrication of GMZ filter

One gram of GZM catalyst was dissolved in ethyl alcohol and sonicated for 15 min with non-woven fabric. Then fiber was packed between two layers of aluminum foil and heated with a heating plate at 100 °C for 2 min. After removing the aluminum foil layers, the fiber was washed and dried at 80 °C for 30 min. Then fiber was activated at 120 °C for 6 h prior to use as GZM Filter.

Photocatalytic disinfection activity of GZM in solution

We took the Gram-negative bacterium *Escherichia coli* (*E. coli*) as model bacteria for photocatalysis experiments. The *E. coli* was incubated in Luria Broth (LB) media at 37 °C for 20 h to get a cell count of 10^9 CFU mL^{-1}. The *E. coli* cells were collected by centrifugation at 4000 rpm for 10 min. Then washed with saline solution (0.9% (w/v)). This concentration of bacteria treated cells was suspended to cell suspension of 10^7 CFU mL^{-1}. We used the Gradient dilution method in 0.9% (w/v) saline solution. Normally, s type of bacteria solution contains 10^7 CFU mL^{-1} of bacteria count. We added 10 mL of GZM catalyst into 100 mL of photocatalysis reactor quartz tube. The simulated visible light source Xenon lamp of 300 W was used. After 30-min intervals, reaction mixture was taken and the remaining bacteria were calculated by plate count method. The GZM composite powders were tested for their photocatalytic performance in degrading methylene blue under visible light irradiation using a Xenon lamp with a power of 300 W (PLS-SXE300/300UV Beijing Bo Philae technology limited). The intensity of the visible light used was kept constant at 25 mW/cm^2. The mixed suspension was exposed to visible light under ambient conditions and stirring. We simulated irradiation at wavelengths from 400 to 780 nm, with the sample placed at a distance of 10 cm from the light. The GZM composite photocatalyst was dispersed into 40 mL of reactant solution containing 0.03126 mM/L of methylene blue concentration at a concentration of 0.1 mg/mL. The reactant was adsorbed onto the photocatalytic surface by stirring slowly in the dark for 1 h to establish the adsorption/desorption equilibrium. After every 60 min, 2.5 mL of the mixed suspension was extracted for analysis. The residual concentration of methylene blue was monitored by measuring the absorbance (using standard calibration curves) with a UV–vis spectrophotometer (spectrum lab gold S54 Shanghai edge light technology). The photocatalytic degradation

efficiency can be determined by measuring the rate of change in concentration of the chemical reaction under the light (UV/vis).

Photocatalytic air disinfection

We designed a rectangular chamber with a 40 cm length, 40 cm width and approximately 50 cm height that was assumed to be an air duct model. *E. coli* containing aerosols was designed similarly to aerosols generated by human sneezing or coughing with almost particle diameter from 2 to 5 µm. We equipped that model aerosols by nebulizing 10^5 CFU mL^{-1} of *E. coli* suspension that was sprayed into the reaction section at the flow rate of 0.4 mL min^{-1} for 1 min. Our GZM catalyst filter was exposed to undersimulate sunlight for 30 min and then air in the reaction section was sampled at a flow rate of 28.3 L min^{-1}. The photocatalytic air disinfection activity of NWFs (non-woven fabric) was evaluated under the same conditions described above by replacing GZM filter with NWF.

Photocatalytic antibacterial activity of GZM filter (suit)

E. coli-containing aerosols with a diameter of 2–5 µm generated from 10^6 CFU mL^{-1} of bacteria suspension were prepared as model-infected aerosols. The top layer of the GZM Filter suit was exposed to a 0.3 mL min^{-1} of aerosols flow for 5 min and then irradiated by simulated sunlight for 30 min at the density of 100 mW cm^{-2}. After that, each layer of the GZM filter was fully washed with 20 mL 0.9% (w/v) saline solution, respectively. The concentrations of bacteria in the eluent were determined by the standard plate count method. Also, each layer of fiber freshly washed by eluent was incubated in nutrient agar for 20 h at 37 °C for residual analysis of adhered viable cells. There were a series of experiments conducted in the dark at the same situations described above. The antibacterial performance of the commercial suit was assessed under the same conditions described above. All the experiments were repeated three times.

Fluorescent-based cell live/dead test

The cell membrane damage of *E. coli* undersimulated sunlight by the photocatalysis process of the bacterial cells was observed with a fluorescence microscope. The collected samples were studied by a fluorescence microscope (Olympus, FV1000) with × 10 magnification. Bacteria and GZM slurry during photocatalytic treatment was collected and stained with dyes of LIVE/DEAD BBcellProbe™ N01/PI bacterial viability kit according to the manufacturer's protocol. The experiment carried out using a mixture of live bacterial cells are stained by N01 and fluorescent green, whereas PI penetrates only damaged membranes and stains of the dead bacterial cells.

Theoretical calculations

Simulation of catalyst by VASTA cif file (with and without defects), DFT electron density map visualization (CrystalExplorer 21.5) and Fourier mapping (Xpert high score plus).

Physical characterization

Powder X-ray diffraction was obtained (XRD, D-MAX2500) to identify the crystal phase. Cu target (Cu $K\alpha = 1.5418$ 10 to 80° was used. The particle size and morphology of the powder were observed by transmission electron microscopy with JEM-2100F operating at 200 kV. The UV–vis spectra were recorded in the range from 200 to 800 nm by Perkin Elmer UV Lambda 900 spectrophotometer. The defect densities of the photocatalyst were measured by the X-ray photoelectron spectrum (XPS) (PHI-5000, US). The binding energies were calibrated by the C1s peak at 284.6 eV. Electrochemical characterization. The electrochemical impedance spectroscopy (EIS) measurements were conducted at open circuit potential using CS350 Electrochemical Workstation in the frequency range from 0.01 Hz to 100 kHz by superimposing an AC voltage of 10 mV amplitude. The electron paramagnetic resonance (EPR) spectrometer settings in a standard photochemical experiment were microwave frequency, ~ 9.424 GHz; microwave power, 10.53 mW; center field, 335.6 mT; sweep width, 8–16 mT; gain, 1×10^5 to 1×10^6; modulation amplitude, 0.05–0.1 mT; scan, 20 s; time constant, 10.24 ms. The g-values (± 0.0001) were determined using a built-in magnetometer. The changes in surface area and porosity resulting from annealing temperature were examined using nitrogen adsorption/desorption analysis (BET) on a Micrometrics ASAP 2020 instrument. Prior to conducting the measurements, the samples underwent degassing at 200 °C for 20 min under a pressure of 0 to 950 mmHg. The concentration of H_2O_2 was measured using a fluorescence probe with HPA, which reacts with H_2O_2 to form a fluorescent p-hydroxyphenylacetic acid dimer in the presence of horseradish peroxidase. Samples were collected at different time intervals and filtered using a 0.22 µm membrane to remove the influence of bacteria cells and photocatalysts. The following scavengers were used: sodium chromate (Cr(VI)) at a concentration of 2.5 mM (Sigma, 99.5%) for electron scavenging, superoxide dismutase at a concentration of 400 U mL^{-1} (Sigma, 99%) for scavenging of $\bullet O_2^-$, L-histidine at a concentration of 2.5 mM (Sigma, 99%) for scavenging of $_1O^2$, catalase at a concentration of 300 U mL^{-1} (Sigma) for scavenging of H_2O_2, isopropanol at a concentration of 2.5 mM (Sigma, 99.5%) for scavenging of •OH, and sodium oxalate at a concentration of 2.5 mM

(Sigma, 99.5%) for scavenging of hole. These scavengers were added to the bacteria suspension prior to illumination. The bacterial concentration in the solution was measured at various time intervals using standard spread plating techniques. Each sample was serially diluted and plated in triplicate onto nutrient agar, then incubated at 37 °C for 20 h. A Thermo Fisher ESCALAB 250Xi was used to conduct VB-XPS, with a monochromatic Al Kα X-ray source. Mott-Schottky measurements were conducted using a CHI 760E electrochemical workstation (Shanghai, China) in 0.5 M Na_2SO_4 solution with a standard three-electrode cell. To prepare the working electrodes, the photocatalyst (7 mg) was dispersed in a 0.5% Nafion solution (0.5 mL) using ultrasound to create a slurry, which was then dip-coated onto a FTO glass electrode (2×0.5 cm^2). The counter electrode and reference electrode used were a Pt plate and Ag/AgCl electrode, respectively.

Results and discussion

Characterization

FESEM and TEM results

The TEM (Fig. 1) was used to investigate the morphology of microwave hydrothermal facilitated GZM composites. The crystalline nanoparticles were extensively populated on the sheets of reduced GO in the low-resolution TEM of GZM composites. Figure 1a, showed that nanoparticles were bonded on the surface of reduced graphene oxide, therefore, are highly capable of charge transfer required for photocatalysis. Based on the HRTEM image obtained from pure ZnO nanoparticles (Fig. 1b), it was determined that the d-spacing between two adjacent lattice fringes is approximately 0.241 nm. This value corresponds to the (101) planes of hexagonal wurtzite ZnO (Sankara Reddy et al. 2013). The corresponding typical HRTEM of MoO_3 NPs is shown in (Fig. 1c) with a fringe spacing of 0.39 nm and corresponds to the (100) planes (Chiang and Yeh 2013). The mixed-phase translation to $ZnMoO_3$ due to the microwave hydrothermal process is further confirmed by the fringe spacing of 0.5 nm (Fig. 1d) (Mafa et al. 2019; Jiang et al. 2014). The EDX pattern (Fig. 2) also represents the presence of all the elements, such as carbon (C) (reduced graphene oxide), in addition to the presence of Zn, Mo and O for the GZM Photo-catalyst. The SEM results of GZM composites are given in the supplementary information S1. The physical characteristics of pure ZnO and MoO_3 metal oxides and graphene oxide can be described by their morphology. Specifically, the as-grown ZnO and MoO_3 has spherical structure, while the graphene sample displays sheet like structure (supplementary information S1 a, b and c from the SEM image). Due to these distinct structural features, the GZM composites are composed of spheres on reduced graphene oxide (supplementary information S1 d).

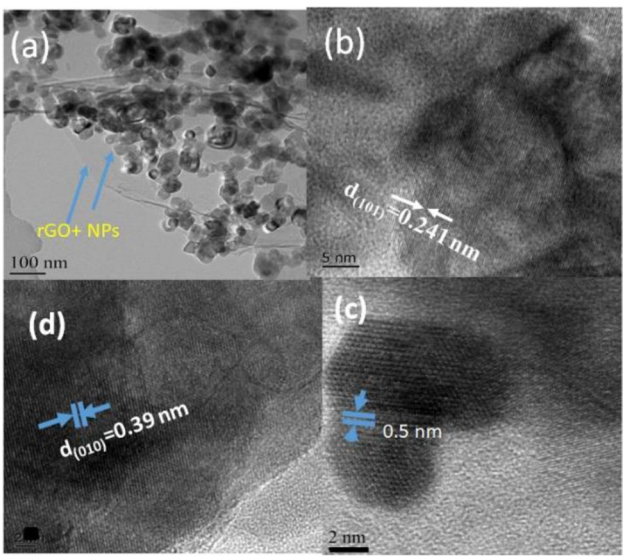

Fig. 1 TEM of GZM composites (**a**), HRTEM image of ZnO nanoparticle showed (101) crystalline planes (**b**), HRTEM of MoO_3 nanoparticles showed (100) crystalline planes (**c**). HRTEM of $ZnMoO_3$ phase detected in composites (**d**)

XRD results

Figure 3a displays the PXRD of the synthesized GZM composites. The diffraction peaks were indexed for the ZnO hexagonal phase of the wurtzite-type, consistent with the literature (JCPDS: 00–003-0752). Figure 3b confirms the phase transition as the MoO_3 peaks partially changed to match those of $ZnMoO_3$ (black peaks). The diffraction peaks demonstrate that the $ZnMoO_3$ NPs consist of multiphase crystals and MoO_3 (reference code: 00–035-0019), confirming that the GZM has a combination of phases. We used microwave hydrothermal treatment of an aqueous (water) solution to synthesize the photocatalysts. The Zn^{2+} (ZnO), and $(MoO_4)^{2-}$ from MoO_3, combined to make GZM composites with new phase $ZnMoO_3$. These ions interacted and created new bonds with the graphene oxide. The peaks of single-layer reduced graphene oxide disappeared, indicating the reduction of GO into rGO and complete coverage by the NPs. The XRD of rGO and GO is provided in the supplementary information (S2) for reference. As peaks had not appeared in XRD, so the results were separately placed in the supplementary information (S2) and further confirmed in RAMAN spectra.

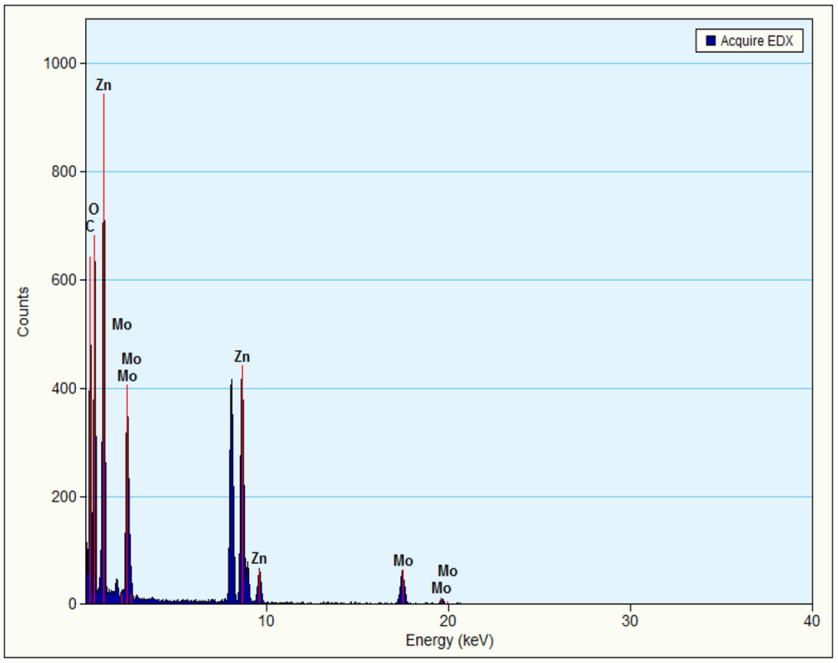

Fig. 2 EDX pattern of GZM catalyst with C, O, Mo, Zn elements

RAMAN results

The Raman spectra of GZM composites showed similar G and D bands structure of carbon, signifying that the structure of graphene was preserved in the composite. The GZM material as produced has two peaks around 1356 and 1604 cm^{-1} (Fig. 3c). At 342 cm^{-1}, the ZnO may be seen. The symmetric stretch of bonds $(\leftarrow O \leftarrow Mo \rightarrow O \rightarrow)$ is attributed to the minority mixed-phase MoO_3 peaks from Raman (A2g) mode, which correspond to the peak situated at

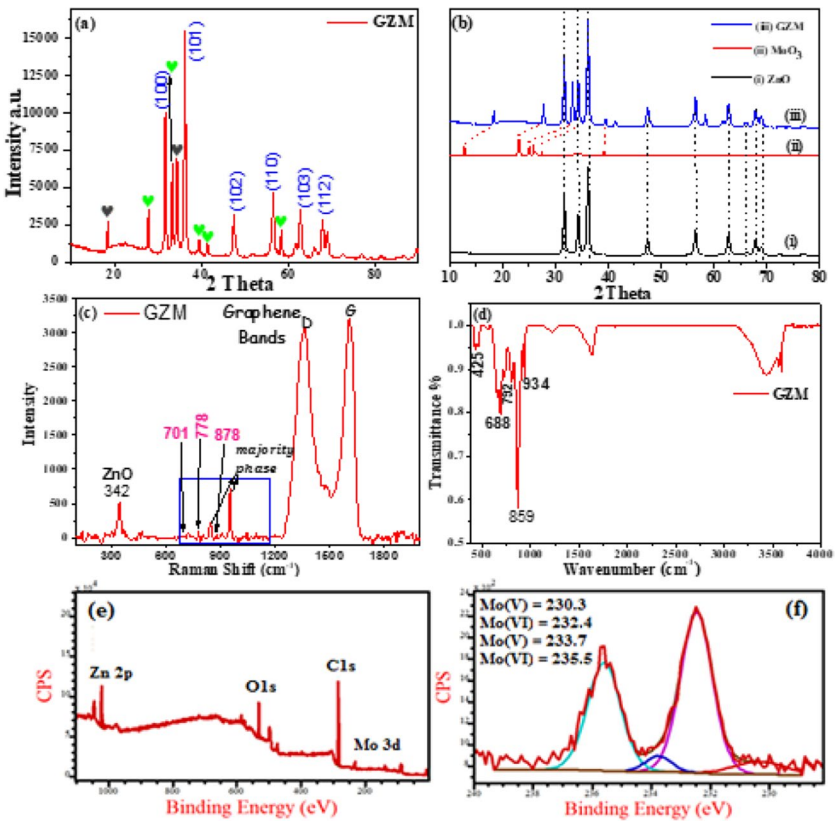

Fig. 3 XRD diffractograms of the (ZnO-MoO_3-$ZnMoO_3$)@ graphene (GZM composites) MoO_3 (marked green) and $ZnMoO_3$(marked black) (**a**), comparison of three XRD patterns ZnO (i), MoO_3 (ii) and GZM (iii) with the peak shift red dotted lines for MoO_3 to $ZnMoO_3$ mixed phase (**b**). RAMAN spectra of GZM composites (**c**). FTIR result for GZM composites. XPS survey spectrum (**e**), XPS spectra of 3d core level regions of Mo^{6+} and Mo^{5+}(**f**)

about 878 cm^{-1} (Fig. 3c). The asymmetric stretch of bonds ($\leftarrow O \leftarrow Mo \rightarrow O \rightarrow$) also gave two Raman (A1g and B1g) modes at 778 and 701 cm^{-1}, respectively. Furthermore, the Mo–O-Mo, Mo = O stretching modes are responsible for the bulk of the molybdenum oxide strong peaks at 943 and 823 cm^{-1}(Xu et al. 2015). The peaks were sharp with higher intensity, indicating the crystallinity of the composites.

FT-IR results

The GZM composite was further characterized by FT-IR spectroscopy. The absorption band of C–OH (3421 cm^{-1}) was greatly reduced (Fig. 3d), which is related to the removal of epoxy and hydroxyl groups linked to the basal graphene. In addition, a novel absorption band at 1217 cm^{-1} was discovered, which corresponded to the establishment of the C–O–Mo bond. The presence of absorption bands of the Zn–O bond was noticed at 425 cm^{-1} in the FT-IR spectra of GZM composites. The major band in the infrared spectra of the minority phase of molybdenum oxide with deformed octahedral [MoO_6] clusters ascribed to an anti-symmetric stretching is about 688 cm^{-1}, which corresponds to an A_u mode. The B_u mode is also linked to a shoulder at 735 cm^{-1}. Lastly, the band at 815 cm^{-1} is associated with the Au mode (Cavalcante et al. 2013), which is attributed to the symmetric stretch of ($\leftarrow O \leftarrow Mo \rightarrow O \rightarrow$) the deformed octahedral [MoO_6] clusters and linear bridging Mo–O–Mo bond with a peak intensity at 860 cm^{-1} and terminal Mo = O at 922 cm^{-1} (Markova-Velichkova et al. 2011).

XPS results

XPS spectra of the Mo3d core level area were examined at room temperature to evaluate the valency of Mo ions, and the result for GZM is given in (Fig. 3e, f) as an example. The binding energies of Mo 3d5/2 and Mo 3d3/2 (spin–orbit components) of Mo^{6+} ions are maxima at 232.4 and 235.5 eV, respectively (Xu et al. 2015). We attempted to evaluate the peak for the $Mo3d_{5/2}$ core level, where the spectrum was fitted using a sum of Gaussian curves (least square method) because the peak is asymmetric. The spectrum was split into two halves, with peaks at 230.3 eV (EB1: low binding energy side) and 233.7 eV (EB2: high binding energy side) (EB2: high binding energy side). The core level of Mo $3d_{5/2}$ is reported to produce a peak at 232.5 eV for Mo^{6+} ions and a peak at 230 eV for Mo^{5+} ions. As a result, it's assumed that Mo ions in GZM are mostly Mo^{6+} ions, with a tiny number of Mo^{5+} ions present as well. XPS core-level regions of C 1 s/2, O1s, Mo 3d/6 and Zn $2p^3$ with XPS quantification report (supplementary information S3). The transformation of GO into rGO was achieved through analysis of the core level XPS spectra of C1s (284.6 eV) in GO and GZM composites. In the presence of ZnO and MoO_3 nanoparticles, supplementary information Fig. (S3a) illustrates that graphene oxide was converted into reduced graphene oxide (rGO), resulting in the disappearance of oxygen functional groups after the microwave treatment. Supplementary information Fig. (S3b) presents the core level XPS spectra of O1s in GZM composites. The major peak is centered at 531.6 eV for GZM composites. In GZM composites, the component located at a lower binding energy of 530.5 eV is attributed to O^{2-} ions, with the intensity of this component indicating the quantity of oxygen atoms in a neighboring fully oxidized stoichiometric state in GZM composites (Kayaci et al. 2014). In the supplementary information, Fig. (S3c) represents the core level spectra of $2p_{1/2}$ and Zn $2p_{3/2}$ for the GZM composites. The peak positions of Zn $2p_{1/2}$ and Zn $2p_{3/2}$ exhibiting an energy difference of 23.1 eV. We were able to observe the high-energy peak at 1023.2 eV attributed to the presence of Zn^{2+} in the hydroxide (Ahmed et al. 2018). XPS quantification report represents the detailed information about atomic mass, atomic concentration and mass concentration of C1s, Zn 2p, O1s and Mo 3d.

EPR and EIS results

The electron paramagnetic resonance (EPR) technique was further performed to elucidate the electronic properties of the MoO_3 and GZM composites (Fig. 4a). The three distinct peaks at g = 1.99, g = 1.98, and gz = 1.91 were observed in the plasmonic MoO_3, which can be attributed to paramagnetic Mo^{5+} centers. Further, thorough considerations of the Mo^{5+} spectrum splitting structure coming from the Zn^{2+} nuclei were observed (Fig. 4b). To explore the importance of these materials in charge separation, EIS analysis (Fig. 5) shows the smallest arc radius that was derived from the MoO_3 sample, which means that better charge transfers and less resistance R_{ct} have been offered by the GZM nanocomposites. The GZM exhibited lower resistance as compared to MoO_3 and rGO–ZnO. The semicircle diameter reduces as a result of irradiation, as does the charge transfer resistance (RCT), which is the impedance to electron transfer across the electrode/electrolyte interface. It can be attributed to ZnO/rGO/MoO_3's robust frameworks and well-defined transport channels. BET results and N_2 adsorption/desorption isotherm at 77 K was used to record the surface area of the samples. According to the multi-point plot, it can be observed that the ZnO and GZM samples exhibit surface areas of 2.1456 and 25.762 $m^2\ g^{-1}$, respectively (supplementary information S4 a, b). Both samples exhibit an isotherm that bears a resemblance to the type IV (IUPAC) isotherm, suggesting that the materials possess mesoporous characteristics (Fig. (b)). The ZnO and GZM samples possess cumulative pore volumes of 0.0216, and 0.0391 $cm^3\ g^{-1}$, respectively.

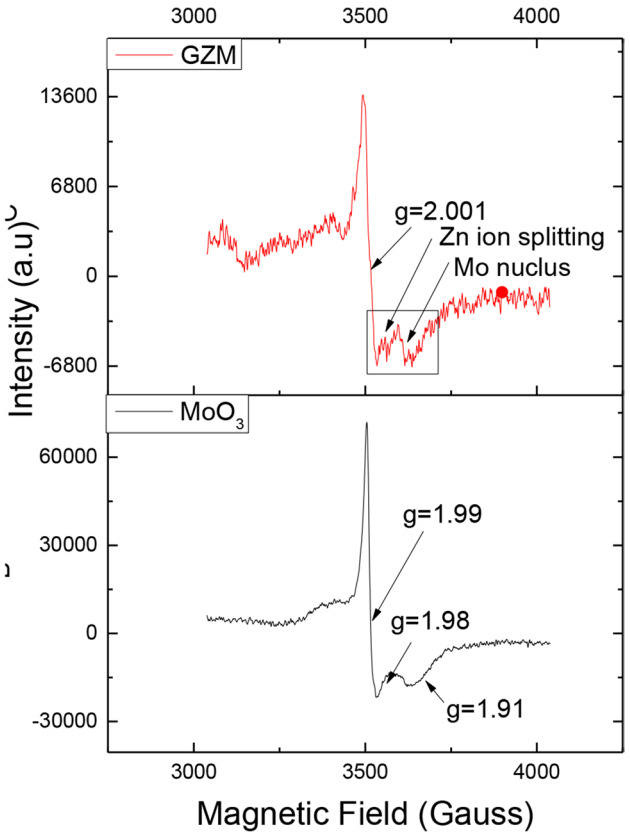

Fig. 4 EPR spectra of MoO_3 (**a**) and GZM (**b**)

Before bacteria inactivation, we checked the Methyl blue (MB) dye photo-degradation in the solution under visible light irradiation. Figure 6a shows the ratio of concentration (C/C_0) change in MB within a certain time and (Fig. 6b) shows the MB degradation peaks in solution. Under visible light exposure, the GZM composites degraded over 76% of the original MB dye in just 4 h.

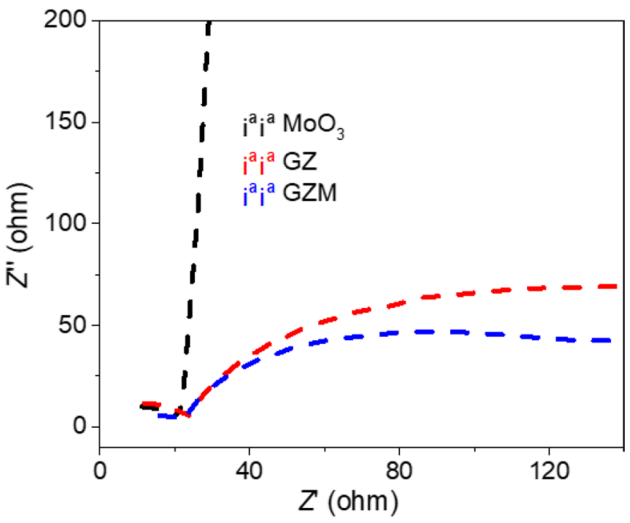

Fig. 5 Nyquist plots, EIS recorded for the MoO_3, GZ and GZM composites

Photocatalytic disinfection performance of GZM

The disinfection studies were carried out in 0.9% (w/v) saline, with an initial *E. coli* cell density of 10^7 colony-forming unit (CFU) mL^{-1} and a catalyst dose of 500 mg L^{-1}. After 120 min of light irradiation, GZM nearly completely inactivates *E. coli* (inactivation efficiency of > 99.99%, equivalent to 6.1, $-\log_{10}(C/C_0)$, but the light only and GMZ in the darkness both have insignificant harmful effects on *E. coli* over the similar period (Fig. 6c). The antibacterial efficacy was shown to be significantly reliant on the GZM dose. We also reduced *E. coli* by 99.99% by reducing the catalyst dose to 300 mg L^{-1} (Fig. 6d). Furthermore, GZM's photocatalytic disinfection activity was compared to that of two typical semi-conductive photocatalysts, anatase TiO_2 and ZnO (ESI-Fig. S6). GZM is more effective than the two compounds mentioned above. When compared to ZnO and anatase TiO_2, the log (inactivation efficiency) of GZM is three and four times greater after 120 min.

Antibacterial performance of GZM filter suit

We used a basic piece of personal protective equipment (PPE) like a non-woven fabric garment to show the potential uses of the GZM filter. The self-cleaning performance of the GZM filter suit was compared with that of a commercial suit (Fig. 7). Pathogenic aerosols created by *E. coli* suspensions were utilized by the suit (5 min). We made three layers (top, middle and bottom) for the suit and the top layer of the suit was exposed to the artificial pathogenic aerosols produced from the *E. coli* suspension for five min. After 1 h of sunlight exposure, we observed a significant quantity of bacteria flourishing on the commercially available non-woven fabric and on each layer of the GZM filter, the quantity of live bacterial cells decreased dramatically, with essentially no quantifiable amounts of living bacteria remaining. These layers were washed with saline solution to visualize live and dead bacteria. As a result, in the control experiment, germs were destroyed by light. The high bactericidal activity of the GZM filter suggests that it has a good protective layer. Experiments were conducted with three layers, but we found that the double-layer suit is better for practical application. To corroborate the light-induced bacteria-killing activity of GZM, fluorescence experiments of *E. coli* cells with various illuminating times were performed (Fig. 7a, b, c). The top layer of the GZM filter was observed at 0 min, 30 min and 60 min. Figure 7a shows live cells green (0 min), intermediate stage green and red (30 min) and dead cells red (60 min), respectively. The *E. coli* colony growth and optical microscope images are shown in the supplementary information S7.

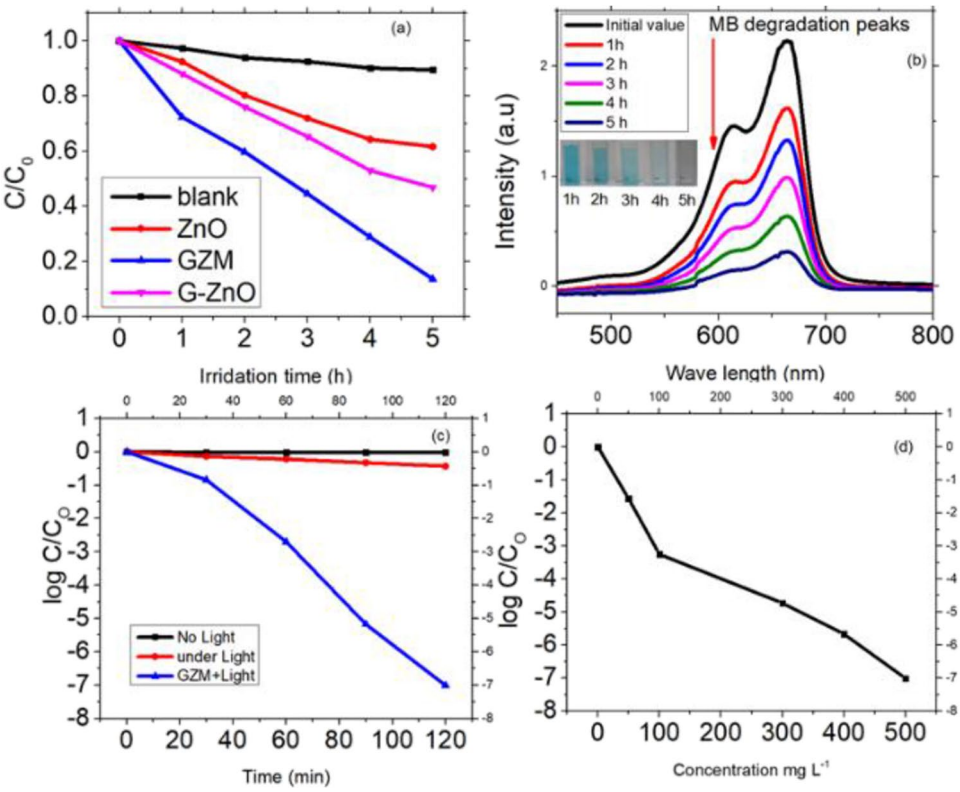

Fig. 6 Photocatalytic degradation of MB under visible light (**a**), MB degradation peaks (**b**), inactivation kinetics of *E. coli* in the presence of GZM (**c**), Photocatalytic disinfection performance of GZM at different dosage levels (**d**)

Theoretical study

Figure 8a, c shows the simulated model of the GZM catalyst with and without defects, respectively. The electron density for the catalyst (Fig. 8b, d) showed deeper electron density for the Mo sites (blue, Fig. 8b) without defects model. We found poorly ordered density for the Mo, Zn and O sites (Fig. 8d), with a significant difference in the electron density around these sub-sites. These DFT results confirmed that the catalyst generated trap sites for photocatalysis. These sites are important to retain a sufficient level of separated electrons and holes by preventing them from recombination, thereby enhancing the photocatalysis process. We further calculated the values for electron density by Fourier mapping (supplementary information S5) for both models (with and without defects). Computed electron density maps (F_{obs}-F_{calc}), or difference Fourier maps showing changes in electron distribution (supplementary information Tables S1 and S2). An X-ray crystallographic experiment (Xpert High Score Plus) produced electron density maps and a complete set of values of electron density for the average unit cell of the catalyst with and without defects F_{obs}-F_{calc} because

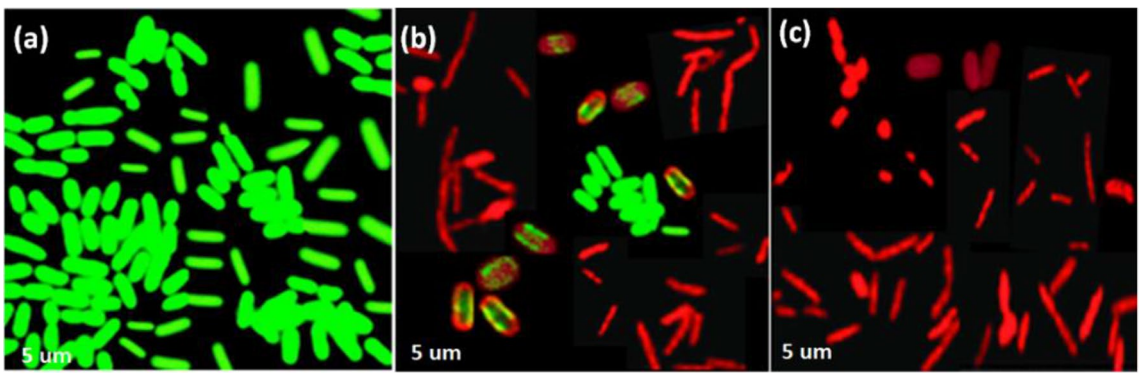

Fig. 7 Confocal fluorescence images of *E. coli* stained with N01 (live cells, green fluorescence) and PI (dead cells, red fluorescence), after cells photocatalytically treated by GZM (500 mg L^{-1}) under sunlight irradiation for 0 min (**a**), 30 min (**b**) and 60 min (**c**) respectively

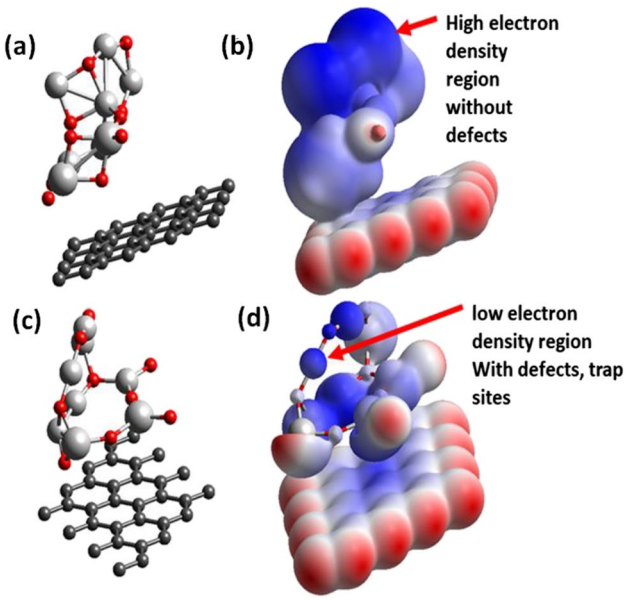

Fig. 8 Simulated catalyst without defects (**a**) and with defects (**c**). Electron density isosurface plots using d_{norm} (**b**, **d**)

the calculation involves combining the observed diffraction data Fo, with the diffraction data calculated from the catalyst model. The highest density was 5.228 between the closest atoms Zn_1 and Zn_2 (without defects model) catalyst (Table S1). The electron density shift was 5.598 towards O_4 and Mo_2 for the closest atoms (defective catalyst model, Table S2). The complete set of values for the electron density with gradual change is given in the supplementary Tables S1 and S2.

Band-structure characterization, photocatalytic disinfection mechanism of GZM and reusability

The photocatalytic mechanism of GZM was investigated by the known methods. The semiconductor properties of GZM were characterized (band structure) to explore the photocatalytic disinfection efficiency and mechanism. GZM exhibited two absorption peaks at 206 and 362 nm, respectively (Fig. 9a). The absorption peak of ZnO at 206 nm can be attributed to the intra-ligand charge transfer and displays a slight red-shift in comparison to the GZM. The broader absorption peak at a longer wavelength of 362 nm is due to ligand to metal charge transfer (LMCT). Bandgap energy

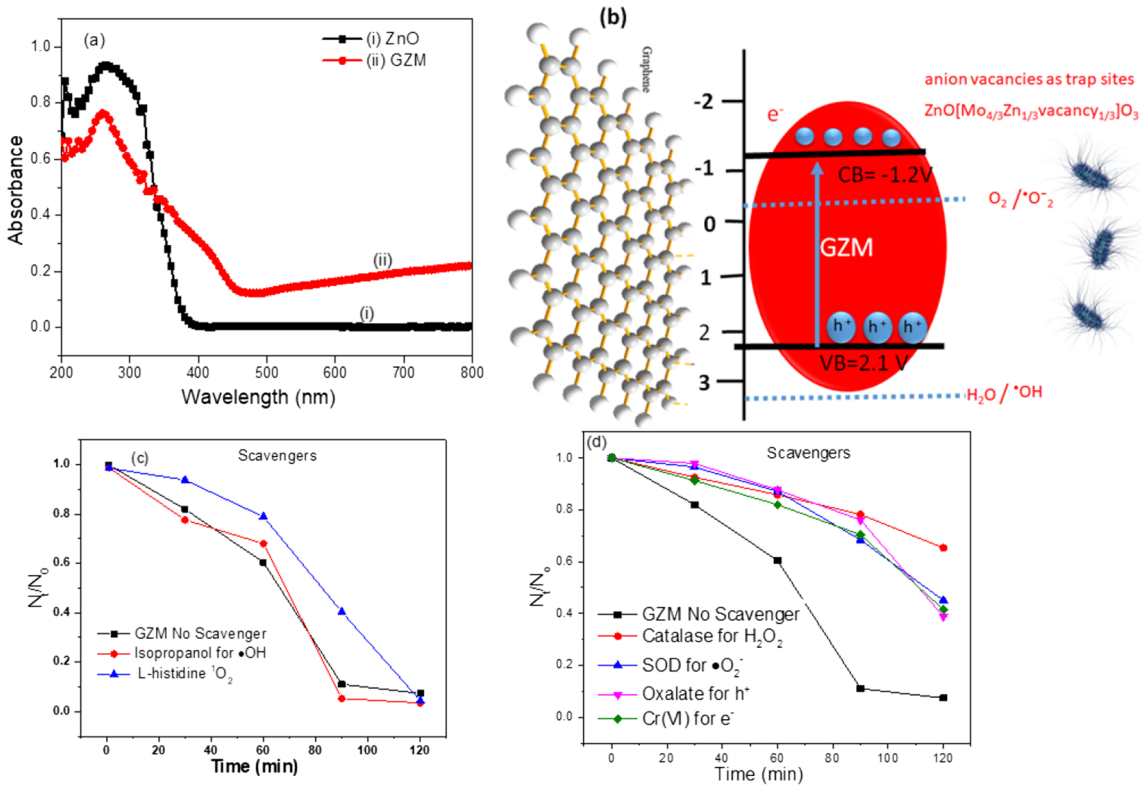

Fig. 9 Band-structure and photocatalytic *E. coli* inactivation mechanism of GZM Composites. **a** UV – vis diffuse reflectance spectra of ZnO and GZM. **b** The band positions of GZM Composites with respect to the reactive oxygen species (ROS) formation potential. **c** the ratio of live to total cells (N_t/N_0) versus the time Photocatalytic disinfection performance with scavenger isopropanol to quench photo generated •OH and L-histidine to quench photo generated $^1O_2$. **d** Catalase to quench photo generated H_2O_2, SOD to quench photo generated $\bullet O^{2-}$, sodium oxalate to quench photo generated h^+, sodium chromate to quench photo generated e^-

was estimated 3.32 eV. The Mott-Schottky measurements were performed at three distinct frequencies and indicated the *n*-type semiconductor nature of GZM. The flat band position of GZM was observed to be approximately − 1.2 V vs. NHE, which corresponds to the bottom of the conduction band (supplementary information S9). It was further demonstrated by VB-XPS (supplementary information S8). The schematic band position of GZM along with ROS reaction potential was illustrated in photocatalytic bacterial inactivation mechanism (Fig. 9b). We further used p-hydroxyphenylacetic acid (HPA) as a probe for the H_2O_2, and the photocatalytic system produced approximately 5.9 µM of H_2O_2 in total over a period of 120 min (supplementary information S10). According to scavenger quenching experiments, H_2O_2 was found to have the most significant impact in causing damage to bacteria and was therefore considered to be the primary active species responsible for this effect. Figure 9c shows the ratio of live to total cells (N_t/N_0) versus the time photocatalytic disinfection performance with scavenger isopropanol to quench photo generated •OH and L-histidine to quench photo generated $^1O_2$. The first-order disinfection rate on GZM with scavengers (IPA → •OH, L-His → $^1O_2$ (supplementary information S11). Figure 9d shows catalase to quench photo generated H_2O_2, SOD to quench photo generated $\bullet O^{2-}$, sodium oxalate to quench photo generated h^+, sodium chromate to quench photo generated e^-. Active species first-order disinfection rate on GZM with scavengers CAT → H_2O_2, SOD → $\bullet O_2^-$, Oxalate → h^+, Cr(VI) → e^- (supplementary information S12). So, the major active species were found according to Fig. 9d. The H_2O_2 was produced at the GZM reduction sites that followed following oxygen reduction pathway as:

$$O_2 + 2H^+ + 2e^- \rightarrow H_2O_2 \text{ at } +0.694 \text{ V vs. SHE}$$

Disproportionation reaction of $\bullet O_2^-$ follows as

$$2 \bullet O_{2^-} + H^+ + H_2O \rightarrow H_2O_2 + O_2 + OH^-, \text{at } +1.43 \text{ V vs. SHE}$$

So the primary species responsible for the photocatalytic *E. coli* inactivation are ROS (H_2O_2 and $\bullet O_2^-$).

Our experiments showed that the GZM filter was able to deactivate 99.99% bacteria in 1 h. The high bactericidal activity of the GZM filter suggests that it provides excellent protection. Comparison with other catalysts Fe_3O_4@SiO_2@ZnO-Ag_3PO, Ag/ZnO@RGO, under the same experimental conditions on the same substrate will be reported in another manuscript. In a previous study, a photocatalyst, Fe_3O_4@SiO_2@ZnO-Ag_3PO (hydrothermal method), was reported with an average performance under visible light. The active species were ·OH, O_2, e^-, and h^+ (Mao et al. 2020). In a second study, Ag/ZnO@RGO was used as the catalyst. The catalyst was effective in inactivating *E. coli* under UV and visible lights (Belachew et al. 2020). The third ZnO/CdS catalyst demonstrated better performance than ordinary ZnO and visible light was used during the process. The active species involved in the reaction were ·OH (Xu et al. 2012). When compared to these reported results, our photocatalyst on PPE showed better performance (supplementary Table S3).

The commercial viability of a photocatalyst depends on reusability and photostability. We used catalyst for 5 cycles of reaction, and the resulting inactivation plots (Fig. 10a) of *E. coli* showed photocatalytic disinfection activity in solution. A gradual decline in inactivation due to the presence of dead bacteria cells was noticed after every cycle until the fifth cycle. During photocatalytic reaction, the solution was periodically removed using a pipette at predetermined time intervals, and the remaining bacterial concentrations were measured using the standard plate count method. The plates were then placed in an incubator at 37 °C for 20 h, and the number of colonies was determined through visual examination. Figure 10b shows repeated cycles of GZM filter with the same result for five cycles. The standard plate count method was used to determine the bacterial concentrations in the eluant. In addition, every layer of the filter that was freshly washed with the eluant was incubated in the nutrient agar at 37 °C for 20 h to analyze the residual viable cells that adhered to it. Similar experiments were also conducted in the absence of light under the same conditions as described earlier.

Active sites of the catalyst and vacancy defects

Based on the XPS and EPR findings, our catalyst exhibited Mo^{5+} species and the existence of two distinct defects, which may act as strong acid sites for the catalytic process of bacterial inactivation. These defects include vacancies in both $ZnMoO_3$ and MoO_3 (Fig. 11). The acid site in the vacancy location of MoO_3 is hypothesized to be responsible for the observed increase in acidity. The deformed MoO_2 generated on the surface of the MoO_3-ZnO catalyst may function as the active site for the metathesis process. Additionally, the microwave-treated graphene oxide utilized in the synthesis process results in a defective layer and acts as trap sites on reduced graphene oxide, further enhancing the catalytic activity of our catalyst. Overall, these findings highlight the important role of defects in the ZnO-MoO_3-$ZnMoO_3$@graphene composites in enhancing their photocatalytic activity and provide valuable insights for further research in this field.

The catalyst used in this study, MoO_3-ZnO@graphene, was found to contain vacancies based on XRD, EPR, and XPS studies. The catalyst surface is composed of MoO_3, and $ZnMoO_3$, with distorted cubic spinel structure with tetrahedral coordination around the molybdenum atom. The $ZnMoO_3$ formula is $ZnO[Mo_{4/3}Zn_{1/3}vacancy_{1/3}]O_3$, where

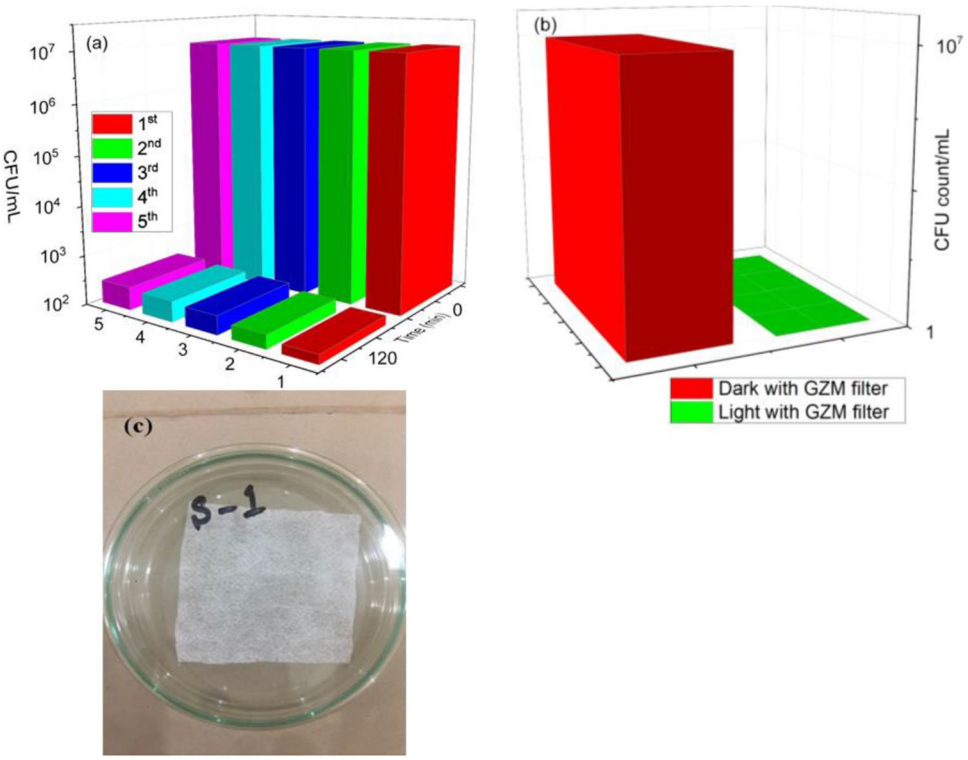

Fig. 10 **a** Reusability of the GZM catalysts for 5 cycles, **b** The quantity of living bacteria collected on a GZM filter using eluent after the photocatalytic reaction was measured in terms of viable cell count. **c** The number of bacterial colonies remaining on the GZM filter treated with eluent after the photocatalytic reaction. These measurements were repeated five times

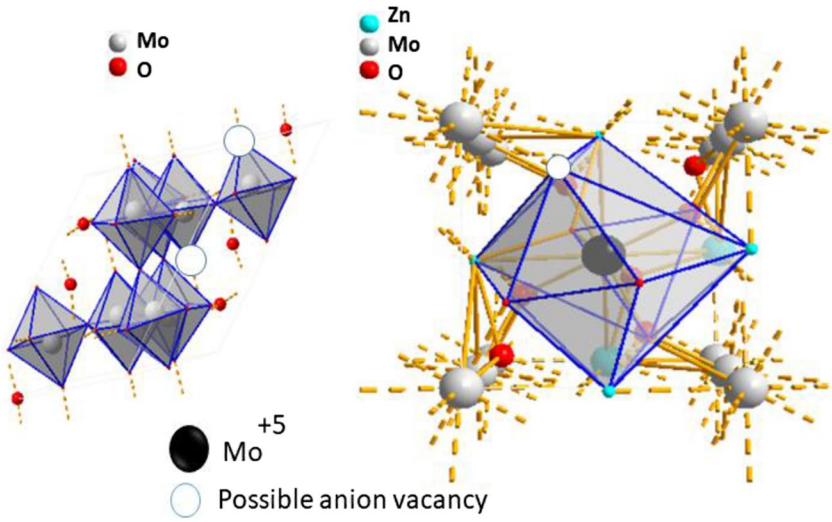

Fig. 11 Active sites of model Photocatalyst, MoO_3 (j) and $ZnMoO_3$ (K)

the increase in surface area may be due to the anion vacancies present in the deformed cubic spinel structure, resulting in an increase in Mo^{5+} levels. The O^{2-} sites are not equivalent, with O^{2-} binding to two equivalent Mo^{4+} and two equivalent Zn^{2+} atoms at the first O^{2-} site, forming deformed corner-sharing OZn_2Mo_2 tetrahedra. The anion vacancy in $ZnMoO_3$ is believed to provide the acid site, as previously reported for hydrogen molybdenum bronze. Therefore, the anion vacancy in $ZnMoO_3$ could play a crucial role in the disinfection activity of the GZM catalyst.

Bacteria can be inactivated by photocatalysts with defect sites on the catalyst. The defect-containing vacancies formed in the MoO_3-ZnO@graphene mixed-phase catalyst, which was confirmed through XRD, EPR, and XPS studies, can act as active sites for bacterial inactivation. The rise in surface area may be due to the deformed cubic spinel structure with anion vacancies, which also leads to an increase in Mo^{5+} levels. The anion vacancy in $ZnMoO_3$ can provide acid sites, which can further enhance the bacterial disinfection activity of the catalyst. The possible mechanism of bacterial

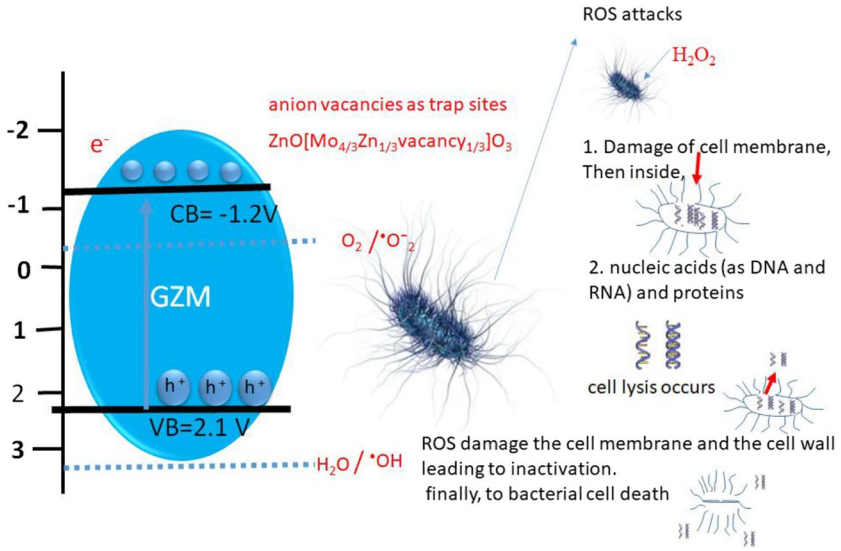

Scheme 2 Photocatalytic *E. coli* inactivation mechanism

inactivation by photocatalysts with defect sites involves the generation of reactive oxygen species, such as hydroxyl radicals, which can damage the cell membranes and cellular components of bacteria, leading to their inactivation. Therefore, the defect sites in the catalyst play an important role in enhancing the photocatalytic activity of the catalyst and can be utilized for effective bacterial disinfection.

The active site for the metathesis process, according to Aritani et al. (1996), deformed MoO_2 generated on the surface of the MoO_3-MgO catalyst. As a result, the deformed MoO_2 on the MoO_3-ZnO catalyst is thought to operate as an active center for the metathesis process, like the MoO_3-MgO catalyst. Furthermore, microwave-treated graphene oxide in the synthesis process also gives a defective layer and acts as trap sites on reduced graphene oxide.

Schematic photocatalytic E. coli inactivation reaction mechanism The photocatalytic reaction is triggered by the excitation of the ZnO-MoO_3-$ZnMoO_3$@graphene photocatalyst by photons, following irradiation by a light source. When the energy of the photons ($E_{hυ}$) is equal to or greater than the bandgap (E_g) (Kenfoud et al. 2021), the electrons (e^-) on the surface of the photocatalyst are excited in the valence band. This excitation causes the electrons to transition to the conduction band, resulting in the formation of an e^- in the conduction band ($e_{CB}-$) and a positive hole in the valence band ($h_{VB}+$). The process described involves a brief period lasting a few femtoseconds, during which the negatively charged electrons in the conduction band (CB) become re-excited and subsequently recombine with the positively charged holes in the valence band (VB) either on the surface or within the bulk of the particle (Baaloudj et al. 2021a, b).

Alternatively, the charge carriers (e^- and h^+) generated can migrate to the surface of the photocatalyst and initiate further redox or oxidation reactions with adsorbed or reactant molecules if they possess sufficient energy or time. The oxidation potential of the reaction between the holes and the reactant molecules should be higher than that of the valence band. In an aqueous environment, the positive holes (h^+) can oxidize water adsorbed at the surface, producing hydroxyl radicals ($^\bullet$OH) which in turn can oxidize organic pollutants, producing carbon dioxide, water, and mineral salts (Byrne et al. 2018). Alternatively, the excited electrons (e −) can quickly reduce the absorbed oxygen on the surface, producing superoxide anion radical (O^{2-}) which can react with (H^+), forming a hydroxyl radical ($^\bullet$OH) that can undergo further oxidation reaction (Chauhan et al. 2018). These concepts are illustrated in Scheme 2.

As approximately 99 wt% of pathogenic microorganisms consist of organic compounds, such as proteins, lipids, lipopolysaccharides, polysaccharides, sugars, amino acids, nucleotides, and nucleic acids (DNA and RNA), these materials can be degraded by photocatalytic substances (Ren et al. 2017). The photocatalyst produces reactive oxygen species (ROS), including $^\bullet$OH, $O_2^{\bullet-}$, HOO$^\bullet$, and H_2O_2 (Ray et al. 2018), which possess potent oxidizing properties for deactivating or killing various waterborne pathogenic microorganisms under ambient conditions (Deng et al. 2020).

Inactivation process follows as: In the first mechanism, reactive oxygen species (ROS) attack the cell membrane and coenzyme A, causing damage to the cell membrane and inhibiting respiration on the cell membrane (Baaloudj et al. 2021a, b). This reduction or prevention of cellular respiration activity leads to cell lysis (Deng et al. 2020). In the second mechanism, the ROS attack the cell membrane and enter the bacterial cell, causing further oxidation of the internal cellular macromolecular components, such as nucleic acids (DNA and RNA) and proteins (Baaloudj et al. 2021a, b). Ultimately, cell lysis occurs. In the last mechanism, the ROS damage both the cell membrane and cell wall, causing the

internal cellular components, such as nucleic acids (such as DNA and RNA), proteins, and some cations, to leak out. This leads to inactivation and, ultimately, the death of the bacterial cell.

Conclusion

The photocatalytic degradation of a model dye (MB) and *E. coli* bacterial disinfection kinetics mediated by the photocatalyst. GZM-PPE coating is presented in this Ms. The GZM-photocatalyst mediated a dye degradation faster compared to ZnO. The innovative composite catalyst prepared by microwave hydrothermal treatment. The ZnO-MoO_3@GO reduced to $ZnMoO_3$ during the preparation process and the vacancy defects seem to be made up by $Zn[Mo_4Zn_{1/3}vacancy_{1/3}]O_{1/3}$ species. The defects acted as active site on the GZM-PPE surface. The second active site was a Mo^{5+} acid site on MoO_3, producing on MoO_3 an anion vacancy. The EPR results showed provided evidence for paramagnetic Mo^{5+} centers and additional split structure coming from the ZnO. An increased charge separation was found by EIS. The electron density of GZM with defect sites was lower compared to GZM. From this observation and the results found by DFT and Fourier mapping, it is possible to suggest that vacancy defects functioned as the active sites during the photocatalytic reaction degrading the dye (MB) and *E. coli*. The GZM-PPE presented an *E. coli* bacterial inactivation activity in acceptable times.

Supplementary information The online version contains supplementary material available at https://doi.org/10.1007/s11356-023-27867-5.

Author contribution **Zongwu Liu**: Conceptualization, Supervision, Investigation Reviewing, and Editing, **Gulzar Ahmed**: Methodology, Writing—Original drafts preparation, **Javid Khan**: Conceptualization, Supervision. **Adeel Rasheed** and **Muhammad Sheraz Ahmed**: Investigation Formal analysis, Reviewing, and Editing, **Khurram Shahzad Munawar:** *E. coli* experiments. **Satesh Bandaru**: DFT Calculations.

Funding No funding for this research.

Data availability All data generated or analyzed during this study are included in this article.

Declarations

Ethics approval No ethical issues were violated in this study.

Consent to participate All authors agree to participate.

Consent for publication All authors agree for publication.

Conflict of interest The authors declare no competing interests.

References

Aritani H, Tanaka T, Funabiki T, Yoshida S, Eda K, Sotani N, Kudo M, Hasegawa S (1996) Study of the local structure of molybdenum− magnesium binary oxides by means of Mo L3-Edge XANES and UV− Vis spectroscopy. J Phys Chem 100:19495–19501

Ahmed G, Hanif M, Zhao L, Hussain M, Khan J, Liu Z (2016) Defect engineering of ZnO nanoparticles by graphene oxide leading to enhanced visible light photocatalysis. J Mol Catal A Chem 425:310–321

Ahmed G, Hanif M, Mahmood K, Yao R, Ning H, Jiao D, Liu Z (2018) Lattice defects of ZnO and hybrids with GO: characterization, EPR and optoelectronic properties. AIP Adv 8(2):025218

Aydin Sevinç B, Hanley L (2010) Antibacterial activity of dental composites containing zinc oxide nanoparticles. J Biomed Mater Res B Appl Biomater 94:22–31

Baaloudj O, Nasrallah N, Kenfoud H, Algethami F, Modwi A, Guesmi A, Assadi AA, Khezami L (2021a) Application of $Bi_{12}ZnO_{20}$ sillenite as an efficient photocatalyst for wastewater treatment: removal of both organic and inorganic compounds. Materials 14:5409

Baaloudj O, Assadi I, Nasrallah N, El A, Khezami L (2021b) Simultaneous removal of antibiotics and inactivation of antibiotic resistant bacteria by photocatalysis: a review. J Water Process Eng 42:10208

Belachew N, Kahsay MH, Tadesse A, Basavaiah K (2020) Green synthesis of reduced graphene oxide grafted Ag/ZnO for photocatalytic abatement of methylene blue and antibacterial activities. J Environ Chem Eng 8:104106

Byrne C, Subramanian G, Pillai SC (2018) Recent advances in photocatalysis for environmental applications. J Environ Chem Eng 6:3531–3555

Chang L, Yan Y, Wang L (2020) Coronavirus disease 2019: coronaviruses and blood safety. Transfus Med Rev 34:75–80

Chauhan A, Rastogi M, Scheier P, Bowen C, Kumar RV, Vaish R (2018) Janus nanostructures for heterogeneous photocatalysis. Appl Phys Rev 5:041111

Choi S-Y, Cho B (2018) Extermination of influenza virus H1N1 by a new visible-light-induced photocatalyst under fluorescent light. Virus Res 248:71–73

Cook T (2020) Personal protective equipment during the coronavirus disease (COVID) 2019 pandemic–a narrative review. Anaesthesia 75:920–927

Chiang TH, Yeh HC (2013) The synthesis of α-MoO_3 by ethylene glycol. Materials 6(10):4609–4625

Cavalcante LS, Moraes E, Almeida MAP, Dalmaschio CJ, Batista NC, Varela JA, Longo E, Siu Li M, Andrés J, Beltrán A (2013) A combined theoretical and experimental study of electronic structure and optical properties of β-ZnMoO4 microcrystals. Polyhedron 54:13–25

Deng Y, Li Z, Tang R, Ouyang K, Liao C, Fang Y, Ding C, Yang L, Su L, Gong D (2020) What will happen when microorganisms "meet" photocatalysts and photocatalysis? Environ Sci Nano 7:702–723

Dhanabal R, Naveena D, Velmathi S, Bose AC (2020) Reduced graphene oxide supported molybdenum oxide hybrid nanocomposites: high performance electrode material for supercapacitor and photocatalytic applications. J Nanosci Nanotechnol 20:4035–4046

Gao P, Ng K, Sun DD (2013) Sulfonated graphene oxide–ZnO–Ag photocatalyst for fast photodegradation and disinfection under visible light. J Hazard Mater 262:826–835

Gopal R, Chinnapan MM, Bojarajan AK, Rotte NK, Ponraj JS, Ganesan R, Gaspar J (2020) Facile synthesis and defect optimization of 2D-layered MoS2 on TiO_2 heterostructure for industrial effluent, wastewater treatments. Sci Rep 10(1):1–15

Huang X, Qi X, Boey F, Zhang H (2012) Graphene-based composites. Chem Soc Rev 41:666–686

Ji J, Bao Y, Liu X, Zhang J, Xing M (2021) Molybdenum-based heterogeneous catalysts for the control of environmental pollutants. EcoMat 3(6):e12155

Jiang YR, Lee WW, Chen KT, Wang MC, Chang KH, Chen CC (2014) Hydrothermal synthesis of β-$ZnMoO_4$ crystals and their photocatalytic degradation of Victoria Blue R and phenol. J Taiwan Inst Chem Eng 45(1):207–218

Kairyte K, Kadys A, Luksiene Z (2013) Antibacterial and antifungal activity of photoactivated ZnO nanoparticles in suspension. J Photochem Photobiol B Biol 128:78–84

Kayaci F, Vempati S, Ozgit-Akgun C, Donmez I, Biyikli N, Uyar T (2014) Selective isolation of the electron or hole in photocatalysis: ZnO–TiO_2 and TiO_2–ZnO core–shell structured heterojunction nanofibers via electrospinning and atomic layer deposition. Nanoscale 6(11):5735–5745

Kenfoud H, Baaloudj O, Nasrallah N, Bagtache R (2021) Structural and electrochemical characterizations of Bi_{12} CoO_{20} sillenite crystals: degradation and reduction of organic and inorganic pollutants. J Mater Sci Mater Electron 32:16411–16420

Kim J, Jang J (2018) Inactivation of airborne viruses using vacuum ultraviolet photocatalysis for a flow-through indoor air purifier with short irradiation time. Aerosol Sci Technol 52:557–566

Kurniawan TA, Mengting Z, Fu D, Yeap SK, Othman MHD, Avtar R, Ouyang T (2020) Functionalizing TiO_2 with graphene oxide for enhancing photocatalytic degradation of methylene blue (MB) in contaminated wastewater. J Environ Manage 270:110871

Lotfi M, Hamblin MR, Rezaei N (2020) COVID-19: transmission, prevention, and potential therapeutic opportunities. Clin Chim Acta 508:254–266

Low J, Yu J, Ho W (2015) Graphene-based photocatalysts for CO_2 reduction to solar fuel. J Phys Chem Lett 6(21):4244–4251

Lu KQ, Li YH, Tang ZR, Xu YJ (2021b) Roles of graphene oxide in heterogeneous photocatalysis. ACS Materials Au 1(1):37–54

Markova-Velichkova M, Iordanova R, Dimitriev Y (2011) Glass formation in the V_2O_5-MoO_3-ZnO system. Phys Status Solidi C 8:3159–3162

Mafa PJ, Ntsendwana B, Mamba BB, Kuvarega AT (2019) Visible light driven $ZnMoO_4$/$BiFeWO_6$/rGO Z-scheme photocatalyst for the degradation of anthraquinonic dye. J Phys Chem C 123(33):20605–20616

Mao K, Zhu Y, Zhang X, Rong J, Qiu F, Chen H, Xu J, Yang D, Zhang T (2020) Effective loading of well-doped ZnO/Ag3PO4 nanohybrids on magnetic core via one step for promoting its photocatalytic antibacterial activity. Colloids Surf A Physicochem Eng Asp 603:125187

Mick P, Murphy R (2020) Aerosol-generating otolaryngology procedures and the need for enhanced PPE during the COVID-19 pandemic: a literature review. J Otolaryngol Head Neck Surg 49:1–10

Morawska L, Tang JW, Bahnfleth W, Bluyssen PM, Boerstra A, Buonanno G, Cao J, Dancer S, Floto A, Franchimon F (2020) How can airborne transmission of COVID-19 indoors be minimised? Environ Int 142:105832

Nakano R, Ishiguro H, Yao Y, Kajioka J, Fujishima A, Sunada K, Minoshima M, Hashimoto K, Kubota Y (2012) Photocatalytic inactivation of influenza virus by titanium dioxide thin film. Photochem Photobiol Sci 11:1293–1298

Ramar V, Karthikeyan B (2021) Effect of reduced graphene oxide on the sunlight-driven photocatalytic activity of rGO/h-MoO3 nanocomposites. J Phys D Appl Phys 54:155502

Ramalingam G, Magdalane CM, Kumar BA, Yuvakkumar R, Ravi G, Jothi AI, Ananth A (2022) Enhanced visible light-driven photocatalytic performance of CdSe nanorods. Environ Res 203:111855

Ray SK, Dhakal D, Regmi C, Yamaguchui T, Lee SW (2018) Inactivation of Staphylococcus aureus in visible light by morphology tuned α-NiMoO4. J Photochem Photobiol A 350:59–68

Ren H, Koshy P, Chen WF, Qi S, Sorrell CC (2017) Photocatalytic materials and technologies for air purification. J Hazard Mater 325:340–366

Suleyman G, Alangaden G, Bardossy AC (2018) The role of environmental contamination in the transmission of nosocomial pathogens and healthcare-associated infections. Curr Infect Dis Rep 20:1–11

Sankara Reddy B, Venkatramana Reddy S, Koteeswara Reddy N (2013) Physical and magnetic properties of (Co, Ag) doped ZnO nanoparticles. J Mater Sci Mater Electron 24:5204–5210

Taghizadeh MT, Siyahi V, Ashassi-Sorkhabi H, Zarrini G (2020) ZnO, AgCl and AgCl/ZnO nanocomposites incorporated chitosan in the form of hydrogel beads for photocatalytic degradation of MB, *E. coli* and S. aureus. Int J Biol Macromol 147:1018–1028

Xu X, Xia F, Zhang L, Gao J (2015) Hydrothermal preparation of MnMoO4/reduced graphene oxide hybrid and its application in energy storage. Sci Adv Mater 7:423–432

Xu F, Yuan Y, Han H, Wu D, Gao Z, Jiang K (2012) Synthesis of ZnO/CdS hierarchical heterostructure with enhanced photocatalytic efficiency under nature sunlight. CrystEngComm 14:3615–3622